

VVV SURVEY MICROLENSING: THE GALACTIC LATITUDE DEPENDENCE

MARÍA GABRIELA NAVARRO ^{1,2,3,*} DANTE MINNITI ^{1,3,4} JOYCE PULLEN ³ RODRIGO CONTRERAS RAMOS ^{3,5}

Departamento de Ciencias Físicas, Facultad de Ciencias Exactas, Universidad Andres Bello, Av. Fernandez Concha 700, Las Condes, Santiago, Chile

Dipartimento di Fisica, Università di Roma La Sapienza, P.le Aldo Moro, 2, I00185 Rome, Italy

Millennium Institute of Astrophysics, Av. Vicuna Mackenna 4860, 782-0436, Santiago, Chile

Vatican Observatory, V00120 Vatican City State, Italy and

Instituto de Astrofísica, Pontificia Universidad Católica de Chile, Av. Vicuna Mackenna 4860, 782-0436 Macul, Santiago, Chile

Not to appear in Nonlearned J., 45.

ABSTRACT

We search for microlensing events in fields along the Galactic minor axis, ranging from the Galactic center to $-3.7 < b < 3.9$ deg., using the VVV survey near-IR photometry. The new search is made across VVV tiles $b291$, $b305$, $b319$, $b347$, $b361$ and $b375$, covering a total area of about 11.5 deg.². We find a total of $N = 238$ new microlensing events in this new area, $N = 74$ of which are classified as bulge red clump (RC) giant sources. Combining them with $N = 122$ events that we had previously reported in the Galactic center (VVV tile $b333$), allows us to study the latitude distribution of the microlensing events reaching the Galactic plane at $b = 0^{\circ}$ for the first time. We find a very strong dependence of the number of microlensing events with Galactic latitude, number that increases rapidly towards the Galactic center by one order of magnitude from $|b| = 2$ deg. to $b = 0$ deg. with a much steeper gradient than with Galactic longitude. The microlensing event population shows a flattened distribution (axial ratio $b/a \approx 1.5$). The final sample shows a shorter mean timescale distribution than the Galactic plane sample for both, the complete population and RC stars.

Keywords: galaxy: bulge — galaxy: structure — gravitational lensing: micro

1. INTRODUCTION

Due to the high stellar density, the bulge of the Milky Way is an ideal place to search for microlensing events (Paczyński 1986). For more than 25 years there have been several optical microlensing experiments that have monitored the Galactic bulge: the Optical Gravitational Lensing Experiment (OGLE; Udalski et al. 1993), Massive Astrophysical Compact Halo Objects (MACHO; Alcock et al. 1993), the Microlensing Observations in Astrophysics (MOA; Bond et al. 2001), the Expérience pour la Recherche d’Objets Sombres (EROS; Aubourg et al. 1993), the Disk Unseen Objects (DUO; Alard et al. 1995a), and the Korea Microlensing Telescope Network (KMTNet; Kim et al. 2010, Kim et al. 2017).

These surveys, however, are incomplete in the Galactic plane because of heavy crowding and extinction. Gould et al. (1995) advocated K -band microlensing in the innermost regions of the Galaxy, clearly outlining the advantages of such surveys, especially the ability to observe through the dust found in large quantities in that area. There are now two new near-IR microlensing searches: one based on the United Kingdom Infrared Telescope Survey (UKIRT, Shvartzvald et al. 2017) in the Northern hemisphere, and the one based on the VISTA Survey Telescope in the Southern hemisphere, that is carrying out the VVV survey (Minniti et al. 2010; Navarro et al. 2017). Both are mapping the inner regions of our Galaxy, that have so far remained hidden from the optical experiments.

The first VVV microlensing events in the Galactic center region were published by Navarro et al. (2017), where a clear excess of microlensing events towards the Galactic

center was found. The Galactic longitude dependence of microlensing along the plane was then studied in Navarro et al. (2018), where 14 VVV tiles ranging from $l = -10$ to $l = 10.44$ deg. were analyse, within a total area covering 20.7 deg.² (Figure 1). The final sample was $N = 630$ microlensing events between the years 2010 and 2015, that exhibit a wide and asymmetric distribution with more events towards negative Galactic longitudes, as predicted by the models of Han & Gould (1995), as a consequence of the barred bulge structure.

All models computed for the Galactic bulge predict that the rates of microlensing events –and therefore the optical depth– increase with decreasing latitude (e.g. Han & Gould (1995), Han & Gould (2003), Wood & Mao (2005), Ryu et al. (2008), Kerins et al. (2009), Penny et al. (2013), Henderson et al. (2014), Wegg et al. (2016), Henderson & Schvartzvald (2016), Poleski (2016), Penny et al. (2018)). This reflects the increasing stellar density as one approaches the Galactic plane. All these models are fine tuned to be in reasonable agreement with the observations from the microlensing optical surveys listed above. These surveys, however, do not reach the Galactic plane, extending only to latitudes $|b| > 2$ deg., and therefore the predictions for the models at $b = 0$ deg. could not be contrasted with observations so far.

In this paper we complement these studies by dealing with the latitude dependence of microlensing, by analyzing six more VVV tiles. They cover an area along the Galactic minor axis ($-1.25 < l < 0.26$ deg.), ranging from $b = -3.7$ to $b = 3.9$ deg., making it now possible to bridge the gap from the optical surveys (Figure 1). This study of the microlensing latitude dependence is also complementary to the microlensing events studied

* Corresponding author: mariagabriela.navarro@uniroma1.it

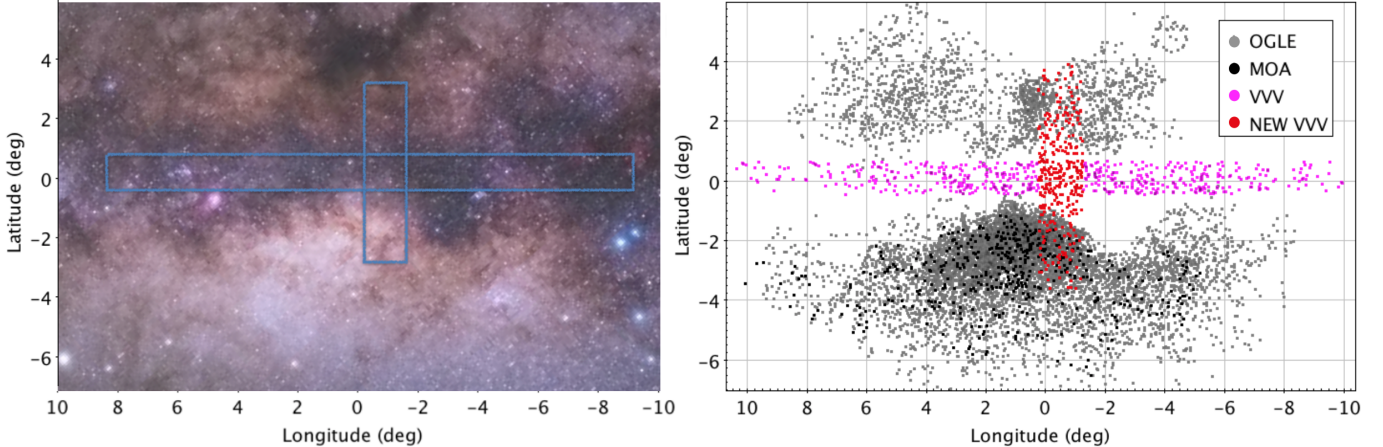


Figure 1. Left panel: Areas mapped by Navarro et al. (2018) along the Galactic plane, and by the present work along the Galactic minor axis, overlaid on the optical image of the Galactic bulge from Mellinger (2009). Right panel: Spatial distribution of the new microlensing events (red squares) above and below the Galactic center. The pink squares are the events found in Navarro et al. (2018). The duplicate events in the overlapping VVV areas have been accounted for. The microlensing events from the OGLE EWS and MOA experiments for years 2010 to 2015 are shown for comparison (grey and black squares, respectively). The animation showing the final sample of microlensing events along with the light curves is available online. In the video the left panel shows the real near-IR image of the area analyzed. The flashes reproduce the microlensing events in their specific locations at the relative time when they occurred. The duration and intensity of the flashes are proportional to the timescale and amplification, respectively. The right panel of the video show the light curve variability with time. The colors are linked with the tile where the event were found. The colors are shown in the right part of the image, from yellow tones for the most negative latitudes (tile b291), to purple tones for the most positive latitudes (tile b375). The realtime duration of the video is 123 seconds representing 5 years of observations.

in the Galactic plane at $b = 0$ deg., for $-10 < l < 10.44$ deg. (Navarro et al. 2018).

In Section 1 the detection procedure and analysis are presented. The analysis of the spatial distribution of the new sample and the comparison of our results with other surveys searching in the same area are presented in Section 3. The timescale and distance distributions are discussed in Section 4. Our final conclusions are presented in Section 5.

2. OBSERVATIONS AND METHOD

The PSF photometry has been obtained with DAOPHOT, as described in detail by (Contreras Ramos et al. 2017).

The microlensing event selection procedure is explained in detail by Navarro et al. (2017), Navarro et al. (2018) and Navarro et al. (2019). Briefly, the first step consisted in the detection of the best microlensing event candidates using a quality number as an indicator. The quality number comprise several features such as a constant baseline, an increase and decrease in brightness in a symmetrical way, and the χ^2 of the fit. In this step we also rejected from the final sample the light curves with less than $N = 20$ data points and the light curves with less than $N = 4$ data points during the event. Approximately 20,000 light curves meet these initial criteria. The second step was to visually inspect the events with the best quality number to obtain the final sample. This procedure leave out of the sample the binary events and events with strong parallax effect. The final sample for the six new tiles analyzed consists in $N = 238$ microlensing events (Figure 1). We found that $N = 70$ events were previously detected by OGLE in the overlapped region.

It is more convenient to restrict the sample to RC sources, as they are usually less affected by incompleteness and describe better the microlensing properties in the Milky Way bulge (e.g. Gould et al. (1995), Popowski

et al. (2001), Popowski et al. (2005), Afonso et al. (2003)). Figure 2 shows the near-IR K_s vs $J - K_s$ color-magnitude diagram (CMD) for the 7 VVV tiles (b291, b305, b319, b333, b347, b361 and b375) covering a range of latitudes along the Galactic minor axis. Comparing this CMD with that of the Galactic plane (Figure 8 of Navarro et al. (2018)), the most striking difference is that reddening is much reduced in these fields above and below the Galactic plane. In order to highlight the extreme and irregular reddening of the plane we show the CMD of each tile plotted in different colors (right panel of Figure 2). The CMD of the innermost tile b333 is shown in grey and is the most affected by extinction as expected. The red clump of every CMD is clear and follow the extinction law proposed by Alonso-García et al. (2018).

Left panel of Figure 2 shows the position of the microlensing sources, outlining the selected RC events. For sources fainter than the detection limit in J band, the color was estimated using the color limit in the CMD. When the K_s magnitude from the photometry was not well constrained, we use the baseline magnitude of the K_s light curve. This is the reason why a line of events are formed in the red side of the CMD. The color cut for the red clump selection depend on the tile, due to the different extinction present in each of them.

We use $J - K_s$ in this case but using the $H - K_s$ CMD the results remain the same. Table 1 lists the Galactic coordinates of each tile along the Galactic minor axis, along with the number of total light-curves analysed, total RC sources analyzed, number of events found, and the corresponding numbers of RC events. All of them are presented as raw values and corrected by completeness.

3. SPATIAL DISTRIBUTION ALONG THE GALACTIC MINOR AXIS AND COMPARISON WITH OTHER SURVEYS

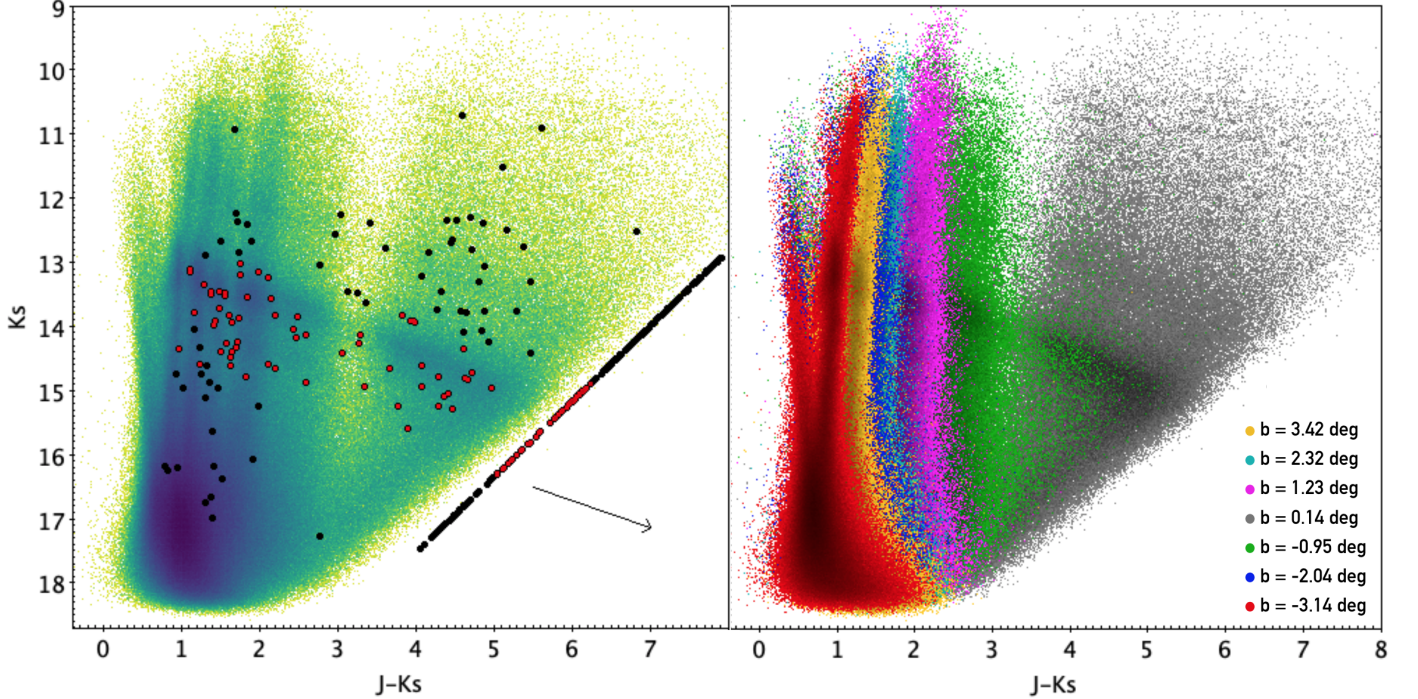


Figure 2. Near-IR K_s vs $J - K_s$ color-magnitude diagrams for the 7 VVV tiles (from $b327$ to $b340$). Left panel: A logarithmic color-coded Hess diagram representation of the ~ 40 million individual sources. The black circles indicate the sources of the sample of microlensing events, and the red circles show the selected RC sources. The line of points to the right of the CMD is due to the events that are only detected in the K_s -band and have no color information, because the sources are too red (i.e. fainter than the detection limits in the J and K_s -bands). The arrow shows the extinction law proposed by Alonso-García et al. (2018) specially computed for the VVV Survey. Right panel: CMDs of the different tiles analysed plotted in different colors along with their central latitudes. The central longitude of all the tiles is $l \sim -0.5$ deg. The dimensions of the tiles are 1.5 deg. and 1.2 deg. for longitude and latitude respectively.

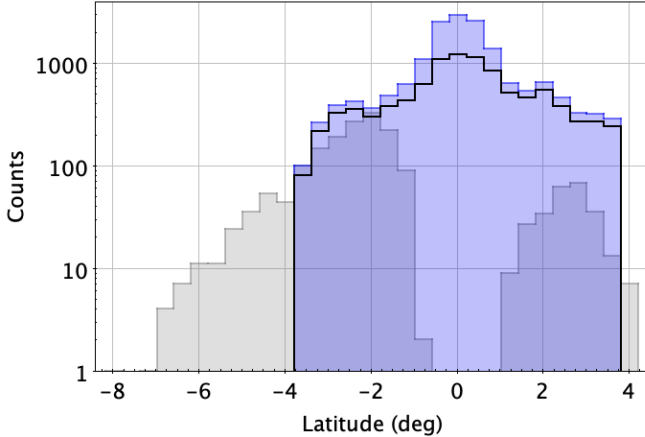


Figure 3. Observed distribution of the total number of microlensing events. OGLE distribution of events found between 2010 and 2015 is shown in grey. The black line shows the raw VVV distribution arbitrarily normalized to the Southern OGLE results in the overlap regions, that have more events. The blue histogram is the distribution corrected by completeness.

The spatial distribution of the complete sample is shown in Figure 1, along with the distribution of events discovered by the OGLE Early Warning System (EWS[†]) and MOA optical surveys between years 2010 and 2015 (Udalski et al. 2015; Sumi et al. 2013). This figure underscores the importance of the VVV survey that completes the microlensing census at low latitudes, where the optimi-

cal surveys are blind because of the high extinction.

It is important to check the number of events compared with OGLE and MOA, in order to obtain an external completeness estimate. Although these different microlensing experiments are not directly comparable, as they all have very different depths, wavelength coverage, and time sampling.

The areal overlap between VVV and OGLE is non uniform, covering approximately 4 deg.² above and below the plane (~ 8.25 deg.² in total). In this common area OGLE detected $N = 1567$ events using the same time baseline (2010 to 2015), while we found $N = 179$ events in total, $N = 109$ of them are new discoveries, generally located in regions of high extinction where OGLE has fewer observations. This order of magnitude difference in the number of events is not surprising, considering that OGLE observed by more than an order of magnitude more nights than the VVV survey, with a total mean sampling of about $N = 85$ nights. Additionally, the VVV bulge observations are random, with typical spacing of a few days (1-3 days), but this is heavily field dependent, and of course there are gaps due to weather and the Moon (some fields cannot be observed once a month because the Moon moves along the ecliptic that goes through the bulge), and seasonal gaps (Hempel et al. 2014). Therefore, on average both microlensing experiments reported ~ 2 events per night. But this still means that the VVV survey is only detecting $\sim 10\%$ of the events.

This is important to take into account when designing the microlensing experiment for WFIRST (Green et al.

[†] <http://ogle.astrow.u.edu.pl>

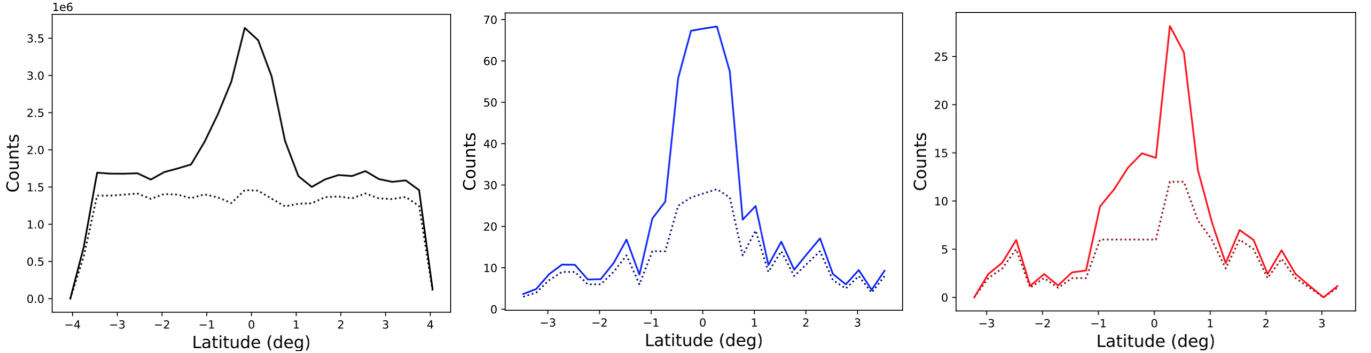


Figure 4. Left: Distribution of the total number of stars (N_{*s}) as a function of latitude. Center: Distribution of the total number of microlensing events ($N_{\mu l}$) as function of Galactic latitude. Right: Distribution of the red clump sample ($N_{\mu l,RC}$) along the Galactic latitude. In all the cases, the dotted line is the raw distribution and the filled line is the completeness corrected distribution (N_{*}^{corr} , $N_{\mu l}^{corr}$, $N_{\mu l,RC}^{corr}$, respectively).

(2012), Spergel et al. (2015)): the potential number of events to be discovered byWFIRST may largely exceed previous expectations if it observes the Galactic center fields. For example, using our measured (raw) latitude dependence distribution, normalised to fit the Southern OGLE region that have more events (black histogram of Figure 3), we find that WFIRST would detect more than $N = 7,000$ events in the Galactic center fields i.e. $|b| \sim 2$ deg. (many more considering that it would be even more efficient than OGLE). Off course this depends on the observational setup, for which it would be very advantageous to extend the WFIRST’s filter from $1.0 - 2.0\mu m$ to $1.0 - 2.4\mu m$ (Penny et al. 2018) or to include a K_s -band filter (Stauffer 2018).

Conversely, in the overlap area with MOA that spans about 2 deg.² they detected $N = 54$ events, while we find $N = 56$ events. They are detecting on average about two events per night.

To make a more accurate analysis of the spatial distribution and its dependence with latitude it is important to consider the completeness corrected distributions. The correction for sampling efficiency does not alter the observed distributions, as the relative number of observations are relatively similar for all VVV survey tiles (e.g. Figure 23 of Navarro et al. (2019)). However, the correction for photometric efficiency is critical, as we move closer to the Galactic center. We apply the completeness corrections following Navarro et al. (2019), that are based on the extensive artificial star simulations of Hempel et al. (2015) and Valenti et al. (2016) using the PSF photometry of Alonso-García et al. (2018). Considering the completeness map for RC stars for stars down to $K_{s0} = 14$ mag, for example, these corrections increase from $\sim 10\%$ for tiles b375 and b291 at $|b| = 3$ deg., to $\sim 50\%$ at the Galactic center tile b333 at $|b| = 0$ deg. The VVV detection limit is field dependent, ranging from $K_s \sim 18$ mag in most fields, to $K_s \sim 16.5$ mag in the Galactic center tile (Saito et al. 2012).

The completeness corrected distribution of the sample is shown in Figure 3 (blue histogram). Using the completeness distribution we expect to find more than $N = 13,000$ events at $|b| \sim 2$ deg.

Figure 4 shows the Galactic latitude distribution of the total number of stars (black), microlensing events (blue) and the number of RC events (red). The observed distributions are shown as dashed lines, while the complete-

ness corrected distributions are plotted as filled lines.

The distribution of the 35 million stars analyzed (left panel of Figure 4) show an increase in the number density of stars that is more peaked when the completeness correction is applied. From Figure 4 we see that the number of microlensing events clearly increases with decreasing latitude, reaching a maximum in the Galactic plane at $b = 0$ deg. There are $N = 181$ total observed events within $-1 < b < 1$ deg. that is the 50% of the sample, while on average there are $N = 89$ observed events with $1 < |b| < 3$ deg., a factor of $2 \times$ less. The respective numbers of events corrected for completeness are $N \sim 390$ within $-1 < b < 1$ deg., and $N \sim 100$ within $1 < |b| < 3$ deg., i.e. a factor of within $3.9 \times$ less.

The effect is even more dramatic if we consider only the RC events, which should be a more complete and unbiased sample in comparison. There are $N = 62$ total observed events within $-1 < b < 1$ deg., while on average there are $N = 25$ observed events with $1 < |b| < 3$ deg., a factor of $2.5 \times$ less. The respective numbers of events corrected for completeness are $N \sim 130$ within $-1 < b < 1$ deg., and $N \sim 30$ within $1 < |b| < 3$ deg., i.e. a factor of within $4.4 \times$ less.

This trend is even clearer in Figure 5 where the corrected distribution of the red clump sample is compared with the microlensing events with RC sources found in Navarro et al. (2018) for the longitude dependence studies. In both cases the number of microlensing events increase towards the Galactic center, but the distribution is wider for the longitude dependence and more pronounced for the latitude dependence. The distribution of the Galactic minor axis sample is fairly symmetric, and more concentrated, while the distribution of the Galactic plane sample is more asymmetric and wider. These distributions have $FWHM = 2.82$ deg. and $FWHM = 9.09$ deg. along latitude and longitude, respectively. In order to be consistent, we limited the sample along the plane within the same area analysed for the latitude dependence ($-3.7 < l < 3.9$ deg.). In this case the distribution has a $FWHM = 4.32$ deg. reflecting that the microlensing events have a flattened distribution (axial ratio $b/a \approx 1.5$) in the innermost regions of the Milky Way, explored here for the first time.

To summarize, we find that the completeness corrected distribution is more peaked, with the number of events strongly increasing when we move from 2 degrees latitude

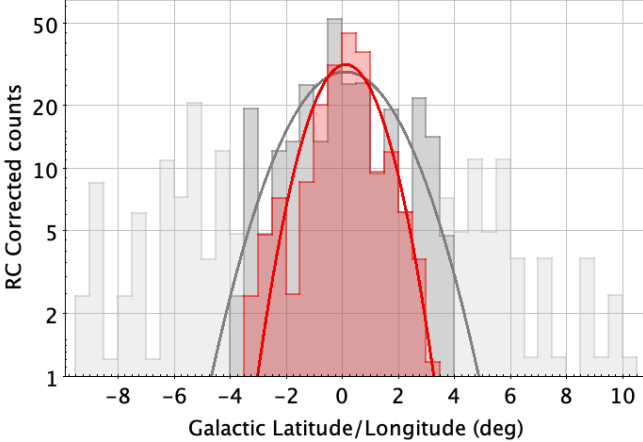


Figure 5. Corrected RC microlensing event distribution along Galactic latitude (red histogram) compared with the corrected distribution of RC events along Galactic longitude (grey histogram) from Navarro et al. (2018). The lines are the Gaussian fit of each distribution. The fit was done within $-3.7 < l < 3.9$ deg. and $-3.7 < b < 3.9$ deg. The $FWHM = 2.82$ deg. and $FWHM = 4.32$ deg. along latitude and longitude samples, respectively.

to zero latitude by a factor of an order of magnitude. As far as we have explored the literature, none of the existing models previously predicted such a large effect.

This has important implications for the microlensing plans for the Wide Field Infrared Space Telescope (WFIRST) mission (Spergel et al. 2015), because most of the selected fields for the WFIRST microlensing campaign are located at $b = -2$ deg. (Penny et al. 2018), thereby missing an important increment in the number of potentially detectable events in comparison with a campaign done at $b = 0$ deg. Additionally, as already pointed out, in order to take better advantage of a microlensing survey in the Galactic plane, an extension of the WFIRST's filter from $1.0 - 2.0\mu m$ to $1.0 - 2.4\mu m$ (Penny et al. 2018) or even better, a K_s -band filter its necessary onboard the WFIRST (Stauffer 2018).

4. TIMESCALE AND DISTANCE DISTRIBUTIONS

The efficiency corrected timescale distribution obtained for the present sample is shown in Figure 6, for both the whole sample and the selected RC sample. The mean timescale for the present sample of events along the Galactic minor axis (excluding the Galactic center i.e. tile b333) is $t_E = 12.8 \pm 1.1$ days, while for the RC sample is $t_E = 18.6 \pm 1.2$ days. The completeness correction was computed using fake microlensing light curves and is explained in detail in Navarro et al. (2019).

As another check for our sample, we can compare the timescale distribution for the events in the new tiles with our previous results published by Navarro et al. (2018) along the Galactic plane at $b = 0$ deg. The events along that Galactic plane have a mean timescale of 17.4 ± 1.0 days for the whole sample of $N = 630$ events, and 20.7 ± 1.0 days for the selected RC sample of $N = 291$ events, respectively (Navarro et al. 2018).

Figure 7 shows the comparison between the raw timescale distribution for the complete sample (blue) and RC sample (red) along the Galactic minor axis and the sample along the Galactic plane from Navarro et al. (2018) (grey). In both cases is clear the shift in the mean

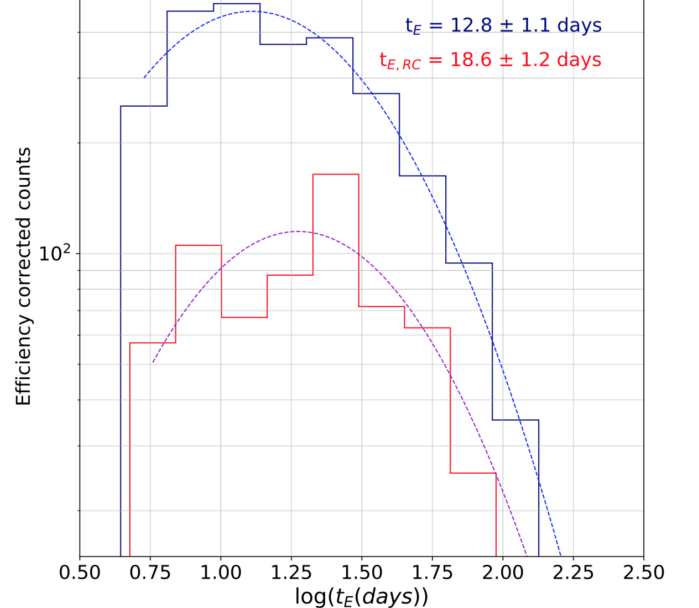


Figure 6. Efficiency corrected timescale distribution for the microlensing sample along the minor axis (blue histogram) and the RC events (red histogram). The mean timescale for the complete sample is $t_E = 12.8 \pm 1.1$ days, while for the RC sample is $t_E = 18.6 \pm 1.2$ days. This distribution exclude the innermost tile b333.

timescale distribution towards shorter timescales.

These observed differences in the mean timescales between the samples along the Galactic minor axis and the Galactic plane are significant at the $4 - 5\sigma$ level. Subtle differences may be expected because the distance distribution of the sources (and therefore the lenses) should be different in these two samples, as the line of sight departs from the Galactic plane.

In both cases (raw and efficiency corrected timescale distributions) the shape of the timescale distribution along the Galactic minor axis (excluding the Galactic center tile i.e. b333) is in good agreement with our previous study of the timescale distribution along the Galactic plane. However, the minor axis sample events have a shorter timescale in the mean than the Galactic plane sample events. This difference is more pronounced for the complete sample than for the RC subsample.

Indeed, Figure 8 shows the comparison of the distance distributions for the RC sources in these two samples. The RC distances are computed using the Gaia RC mean magnitudes and colors from Riuz-Dern (2018), following the method of Navarro et al. (2019). Note that we adopt the mean intrinsic magnitude of the RC to be $K_{s0} = -1.61 \pm 0.01$ (Riuz-Dern 2018), but adopting a different calibration such as $K_{s0} = -1.68 \pm 0.03$ from Alves et al. (2002) or even computing the individual extinctions for all the RC sources using the last version of the BEAM calculator (Gonzalez et al. 2012) does not change our conclusions.

Figure 8 shows that the Galactic minor axis RC sources (red histogram) are mostly located at the distance of the Galactic bulge ($6 < D < 12$ kpc), as expected. On the other hand, the Galactic plane RC sources (grey histogram) are more asymmetric and widely distributed. Their distance distribution peaks at the distance of the

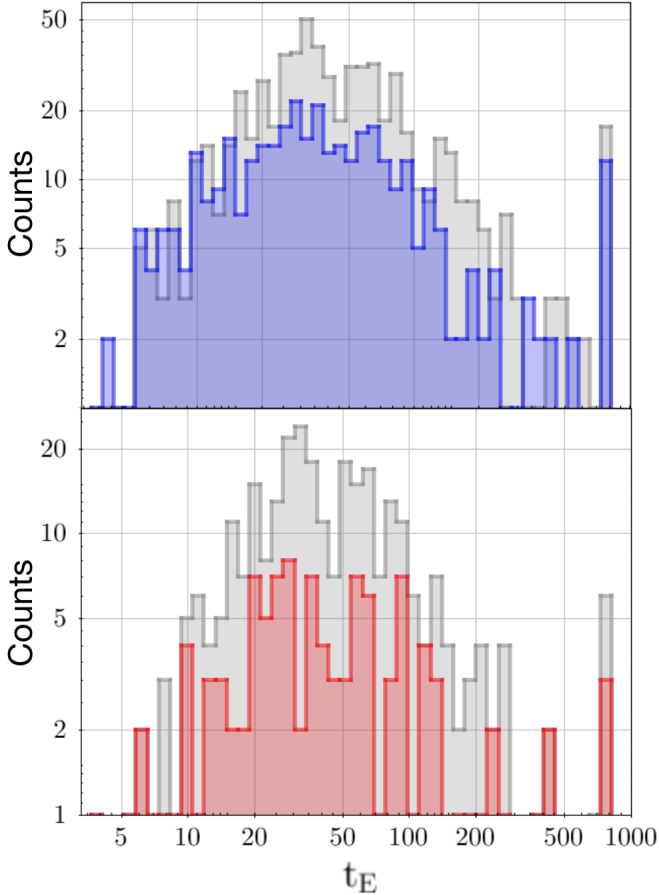


Figure 7. Comparison between the raw timescale distribution for the samples along the Galactic minor axis (blue and red histogram), and major axis (grey histogram, from Navarro et al. (2018)).

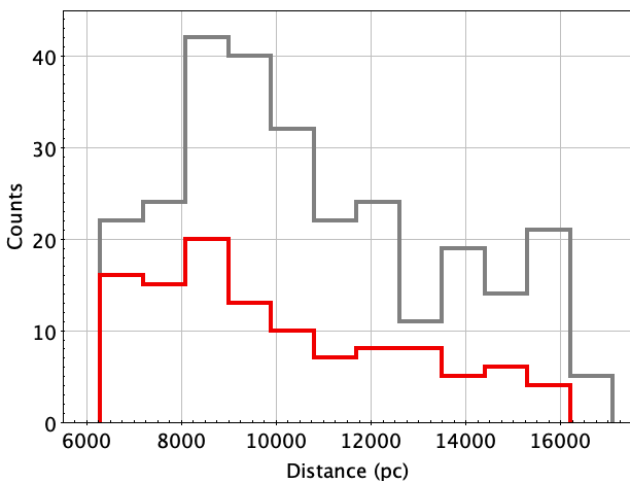


Figure 8. Observed RC microlensing event distance distribution along Galactic latitude (red histogram) compared with the distance distribution of the total number of RC events along Galactic longitude (grey histogram) from Navarro et al. (2018).

Galactic center, but a sizeable fraction of the population (20 – 30%) is clearly located in the background, beyond $D \sim 12$ kpc, including some located at the Galactic antipodes ($D \sim 16$ kpc).

Figure 8 clearly shows that some of the sources of the low latitude microlensing events may be very distant, demonstrating the usefulness of the VVV survey for probing the populations much beyond the Galactic center. However, larger numbers of microlensing events and detailed modeling are needed in order to explore in detail whether the observed difference in distances can explain the difference in timescales between the two samples.

5. CONCLUSIONS

We have detected $N = 238$ microlensing events within an area of 11.5 deg.² along the Galactic minor axis at $l = -0.5$ deg. using the near-IR VVV Survey photometry.

In Navarro et al. (2018) we found that there is an excess of microlensing events at negative longitudes, and that the observed longitude dependence is very shallow, as expected from the model predictions. The latitude dependence however, should be stronger, as also predicted by the models and observed in the higher latitude fields by the optical microlensing surveys.

We find that the Galactic latitude dependence is much stronger than the longitude dependence, which is significantly shallower. The observed number of events drops from $N = 122$ at $b333$ to $N \sim 68$ at $b332$ and $b334$ at 1.5 deg. in longitude (decrease by 41%), (a crude interpolation yields at 1.1 deg. in latitude a decrease by 31%) while they drop from $N = 122$ at $b333$ to $N = 59$ and $N = 56$ at $b319$ and $b347$ respectively, at 1.1 deg. in latitude (decrease by 47%).

The completeness corrected trends highlight the difference more strongly. The differential extinction was taken into account on a field by field basis, if there is any residual effect it would be in the sense of making the real gradient even more pronounced. In other words, because extinction is more severe as one approaches the Galactic plane, the number of events in these regions should be larger than observed.

The $FWHM$ of the distribution is $1.5 \times$ larger along Galactic longitude than along latitude, indicating a highly flattened microlensing event rate distribution in the innermost regions of the Milky Way.

In summary, we find that there is an order of magnitude more microlensing events at $b = 0$ deg. than at $|b| = 2$ deg. This is significantly higher than all the expectations from all the previous models (that were fine tuned to explain the observations from the optical surveys at higher latitudes). The higher event rate observed in the Galactic plane is probably due to a combination of two effects: the higher source density, and the higher microlensing optical depth.

We also find that the mean timescales of the Galactic plane sample from Navarro et al. (2018) is longer than the present sample along the Galactic minor axis, both considering the total samples or the selected RC giant star events. These differences may be due to the different distance distribution of the sources of the microlensing events (and therefore also of the lenses).

We find that the present sample of events along the Galactic minor axis contains fewer distant RC giants located beyond the bulge than the Galactic plane sample

Table 1

Number of VVV Survey Microlensing Events Along the Galactic Minor Axis. The tiles are presented along with the equatorial and Galactic coordinates, the number of sources and red clump sources analyzed and the number of events for the whole sample and the red clump subsample, both raw and corrected by completeness. The subscript “F” indicates that the real number is obtained by multiplying the value by a factor of $\times 10^5$.

Tile	RA(J2000)	DEC(J2000)	l(deg.)	b(deg.)	$N_{*,F}$	$N_{*,F}^{corr}$	$N_{*RC,F}$	$N_{*RC,F}^{corr}$	$N_{\mu l}$	$N_{\mu l}^{corr}$	$N_{\mu l,RC}$	$N_{\mu l,RC}^{corr}$
b291	17 56 53.736	-30 58 01.200	359.50054	-3.13672	53.7	65.2	3.8	4.7	22	26	5	6
b305	17 52 29.424	-30 25 22.080	359.49334	-2.04452	49.2	59.2	6.3	7.6	34	40	10	12
b319	17 48 08.616	-29 51 58.320	359.48996	-0.95233	48.9	77.8	10.8	17.3	59	93	18	28
b333	17 43 51.192	-29 17 52.800	359.48985	0.13988	60.6	144.5	13.7	32.7	122	290	38	90
b347	17 39 37.152	-28 43 06.240	359.49322	1.23206	53.8	64.4	9.4	11.2	56	66	25	29
b361	17 35 26.472	-28 07 39.360	359.50024	2.32421	58.4	71.3	5.8	7.0	42	51	14	17
b375	17 31 19.032	-27 31 34.680	359.51046	3.41635	58.3	67.8	3.4	3.9	25	29	2	2

of Navarro et al. (2018), where the distant RC giants are much more numerous. We argue that larger samples of microlensing events in the direction of the bulge, and detailed modeling are needed to study these trends.

This is the first time a latitude analysis of the microlensing event population is done reaching the Galactic plane at $b = 0$ deg. This study enables more complete future modeling of the microlensing rates and optical depths throughout the Galactic bulge. We also strongly advocate for aWFIRST microlensing campaign along the Galactic plane, where the event rate is clearly maximal.

We gratefully acknowledge the use of data from the ESO Public Survey program IDs 179.B-2002 and 198.B-2004 taken with the VISTA telescope and data products from the Cambridge Astronomical Survey Unit. Support for the authors is provided by the BASAL Center for Astrophysics and Associated Technologies (CATA) through grant AFB 170002, by the Programa Iniciativa Científica Milenio grant IC120009, awarded to the Millennium Institute of Astrophysics (MAS), and by Proyecto FONDECYT No. 1170121.

REFERENCES

- Afonso, C., Albert, J. N., Alard, C., et al. 2003, A&A, 404, 145
 Alcock, C., Akerlof, C. W., Allsman, R. A., et al. 1993, Nature, 365, 621
 Alard, C., Guibert, J., Bienayme, O., et al. 1995, Messenger 80, 31
 Alonso-García, J., Saito, R. K., Hempel, M. et al., 2018, A&A, 619, A4
 Alves, D. R., Rejkuba, M., Minniti, D. & Cook, K. H., 2002, ApJ, 573, L51
 Aubourg, E., Bareyre, P., Brhin, S., et al. 1993, Nature, 365, 623
 Bond, I. A., Abe, F., Dodd, R. J., et al. 2001, MNRAS, 327, 868
 Contreras Ramos, R., Zoccali, M., Rojas, F., et al. 2017, 608, 140
 Gonzalez, O. A., Rejkuba, M., Zoccali, M., et al. 2012, A&A, 543, 13
 Gould, A. 1995, ApJ, 447, 991
 Green, J., Schechter, P., Baltay, C., et al. 2012, arXiv:1208.4012
 Han, C. & Gould, A. 1995, ApJ, 449, 521
 Han, C. & Gould, A., 2003, ApJ, 592, 172
 Hempel, M., Minniti, D., Dekany, I., et al. 2014, The Messenger, 155, 24)
 Hempel, M., et al. 2015, preprint
 Henderson, C. B., Gaudi, S., Han, C., et al., 2014, ApJ, 794, 1
 Henderson, C. B. & Shvartzvald, Y., 2016, AJ, 152, 96
 Kerins, E., Robin, A. C. & Marshall, D. J., 2009, MNRAS, 396, 1202
 Kim, S.-L., Park, B.-G., Lee, C.-U., et al. 2010, Proc. SPIE, 7733, 77733
 Kim, D.-J., Kim, H.-W., Hwang, K.-H., 2017, arXiv:1703.06883
 Mellinger, A., 2009, PASP, 121, 1180
 Minniti D., Lucas, P. W., Emerson, J. et al. 2010, New Astron., 15, 433
 Navarro, M. G., Minniti, D. & Contreras Ramos, R. 2017, ApJ, 851, L13
 Navarro, M. G., Minniti, D. & Contreras Ramos, R. 2018, ApJ, 865, L5
 Navarro, M. G., Minniti, D., Contreras Ramos, R., Pullen, J. B., Capuzzo Dolcetta, R., & Lucas, P. W. 2018, ApJ, submitted arXiv:1907.04339
 Paczyński, B. 1986, ApJ, 304, 1
 Penny, M. T., Kerins, E., Rattenbury, N. et al. 2013, MNRAS, 434, 2
 Penny, M. T., et al. 2018, ApJ, in press (arXiv:1808.02490)
 Poleski, R. 2016, MNRAS, 455, 3656
 Popowski, P., Griest, K., Thomas, C. L., et al. 2005, ApJ, 631, 879
 Popowski, P., Alcock, C., Allsman, R. A. et al., 2001, ASPC, 239, 244P
 L. Ruiz-Dern, C. Babusiaux, F. Arenou, C. Turon, R. Lallement, 2018, A&A, in press (arXiv:1710.05803)
 Ryu, Y. H., Chang, H. Y., Park, M. G., & Lee, K. W. 2008, ApJ, 689, 1078
 Saito, R. K., Hempel, M., Minniti, D., et al. 2012, A&A, 537, A107
 Shvartzvald, Y., Bryden, G., Gould, A., Henderson, C. B., Howell, S. B., & Beichman, C., 2017, MNRAS, 457, 4089
 Smith, L. C., Lucas, P. W., Kurtev, et al. 2018, MNRAS, 474, 1826
 Spergel, D., Gehrels, N., Baltay, C., et al. 2015, arXiv:1503.03757
 Stauffer, J., Helou, G., Benjamin, R., et al. 2018, arXiv:1806.00554
 Sumi, T., Bennett, D. P., Bond, I. A., et al. 2013, ApJ, 778, 150S
 Udalski, A., Szymanski, M., Kaluzny, J., et al. 1993, AcA, 43, 289
 Udalski, A., Szymanski, M., Szymanski, G., 2015, AcA, 65, 1
 Valenti, E., Zoccali, M., Gonzalez, O. A., et al. 2016, A&A, 587, L6
 Wegg, C., Gerhard, O., & Portail, M., 2016, MNRAS, 463, 557
 Wood, A. & Mao, S. 2005, MNRAS, 362, 945

Table 2
 VVV Survey first quality microlensing events with their respective positions
 in Galactic coordinates, baseline K_s magnitude, Color and the parameters
 obtained using the standard microlensing model including the blending (f_{bl}).
 The events with DET were detected by OGLE.

Tile	ID	l (deg.)	b (deg.)	K_s (mag)	$J - K$ (mag)	Amp	u_0	t_0 (MJD)	t_E (days)	f_{bl}	Comment
291	14359	-0.83423	-3.56950	14.34	6.71	1.42	0.36 ± 0.70	57224.73 ± 16.88	71.50 ± 85.47	0.92 ± 2.71	
291	18483	-0.76825	-3.57744	14.23	6.80	0.38	0.53 ± 0.60	55811.60 ± 1.81	37.70 ± 26.38	0.39 ± 0.67	DET.
291	60869	-1.16721	-3.28885	17.46	4.06	12.64	0.06 ± 0.05	56794.68 ± 0.35	115.33 ± 57.01	1.00 ± 0.70	DET.
291	8466	-0.82319	-2.63851	14.13	6.89	0.44	0.86 ± 1.06	56908.31 ± 4.48	69.65 ± 55.27	1.00 ± 2.37	DET.
291	95627	-0.85515	-3.34676	16.20	5.13	5.32	0.00 ± 2.00	56738.29 ± 0.17	750.00 ± 1172.43	0.02 ± 0.03	
291	58006	-0.44430	-2.72898	13.09	7.77	0.13	0.00 ± 2.00	56869.67 ± 2.48	130.01 ± 90.84	0.02 ± 0.02	DET.
291	59043	-0.25578	-2.73065	13.30	7.60	0.29	0.83 ± 2.00	56776.70 ± 2.71	16.77 ± 35.20	1.00 ± 7.04	DET.
291	71521	-0.25151	-2.75399	13.00	7.85	3.23	0.16 ± 0.03	55803.04 ± 0.28	116.91 ± 14.52	0.90 ± 0.18	DET.
291	31045	-1.00208	-3.60150	12.66	8.14	0.22	1.20 ± 1.72	57094.94 ± 7.52	149.73 ± 143.03	1.00 ± 3.27	DET.
291	33760	-0.45070	-3.23385	17.39	4.11	1.78	0.27 ± 0.71	56524.65 ± 4.78	44.40 ± 84.13	0.60 ± 2.09	DET.
291	48672	0.00268	-2.72106	15.41	5.80	0.77	0.00 ± 2.00	56819.98 ± 4.27	750.00 ± 4258.06	0.01 ± 0.04	
291	79253	-0.07317	-3.32179	13.15	7.72	1.98	0.32 ± 0.02	56123.10 ± 0.04	13.95 ± 0.63	0.90 ± 0.08	DET.
291	9436	0.07983	-2.64175	16.74	4.67	4.47	0.08 ± 0.09	56113.04 ± 0.80	13.89 ± 9.56	0.41 ± 0.49	DET.
291	31223	-0.13540	-3.59885	17.08	4.38	1.46	0.00 ± 2.00	56811.82 ± 2.08	31.62 ± 27.70	1.00 ± 1.72	
291	27754	0.19082	-3.04078	15.13	6.04	1.09	0.41 ± 0.21	56013.86 ± 4.04	125.65 ± 37.42	0.67 ± 0.48	DET.
291	36659	0.20795	-3.05757	15.94	5.35	2.37	0.28 ± 0.24	56557.06 ± 0.48	21.66 ± 11.19	1.00 ± 1.03	DET.
291	40922	0.14566	-3.06548	17.19	4.29	2.52	0.16 ± 0.25	56153.07 ± 1.08	33.18 ± 28.89	0.61 ± 0.91	DET.
291	41165	-0.73302	-3.06388	13.74	7.22	0.60	0.65 ± 0.32	56448.53 ± 1.28	107.52 ± 30.31	1.00 ± 0.78	DET.
291	42518	-1.05530	-2.88447	13.24	7.64	0.22	0.00 ± 2.00	56809.20 ± 9.24	12.15 ± 53.86	1.00 ± 13.27	
291	43816	-0.47510	-2.88488	11.97	8.73	2.38	0.00 ± 2.00	56402.71 ± 4.54	351.68 ± 97.48	0.15 ± 0.06	DET.
291	15478	-0.08828	-2.83466	15.26	5.93	1.01	0.46 ± 0.48	56149.96 ± 0.59	25.12 ± 15.45	0.86 ± 1.26	DET.
291	87991	-0.02270	-2.97132	13.32	7.58	0.74	0.66 ± 0.20	56153.43 ± 0.28	33.58 ± 6.57	1.00 ± 0.51	DET.
305	51721	-1.13552	-1.99593	13.59	7.34	0.34	0.56 ± 2.00	56149.91 ± 0.42	6.60 ± 13.10	1.00 ± 6.45	DET.
305	58739	-0.69976	-2.55682	15.19	5.99	1.62	0.07 ± 0.05	56840.22 ± 0.09	18.99 ± 11.10	0.13 ± 0.09	DET.
305	102736	-0.82319	-2.63851	14.11	6.90	0.43	0.86 ± 0.87	56910.29 ± 4.67	78.95 ± 49.93	1.00 ± 1.93	
305	5363	-0.86367	-1.54147	13.59	7.35	0.32	1.02 ± 2.00	55811.96 ± 1.92	32.05 ± 71.55	1.00 ± 7.03	
305	28573	-0.82439	-2.13497	13.83	7.15	0.26	0.11 ± 2.00	56880.04 ± 5.65	18.52 ± 106.53	1.00 ± 21.02	DET.
305	44942	-0.34826	-1.61946	14.06	6.95	0.32	0.27 ± 1.98	56534.28 ± 2.31	47.94 ± 217.16	0.15 ± 1.28	DET.
305	89982	-1.23501	-1.89040	13.59	7.35	3.95	0.20 ± 0.03	56117.73 ± 0.10	25.88 ± 2.40	1.00 ± 0.16	
305	40818	-0.73734	-1.79001	16.70	4.70	2.53	0.19 ± 0.33	56369.75 ± 0.26	21.58 ± 30.71	0.62 ± 1.29	DET.
305	72856	-0.81026	-1.85066	16.87	4.56	2.01	0.23 ± 0.70	56863.31 ± 6.36	41.16 ± 70.79	1.00 ± 3.48	DET.
305	27319	-0.87610	-2.31628	12.63	8.16	0.40	0.86 ± 2.00	55848.44 ± 0.84	14.60 ± 64.20	1.00 ± 14.33	
305	64527	-1.01654	-1.83685	13.05	7.81	0.15	0.00 ± 2.00	55927.89 ± 2.98	106.95 ± 74.85	0.16 ± 0.30	
305	40638	-0.91480	-2.34845	13.90	7.08	2.05	0.29 ± 0.04	56096.17 ± 0.34	61.13 ± 5.51	0.82 ± 0.14	DET.
305	67899	-0.61263	-1.83984	14.46	6.61	5.04	0.11 ± 0.01	55808.83 ± 0.10	87.81 ± 6.58	1.00 ± 0.11	DET.
305	66801	-0.56543	-2.38898	15.33	5.87	2.70	0.27 ± 0.38	55788.67 ± 2.30	31.04 ± 23.15	1.00 ± 1.66	DET.
305	75109	-0.67287	-2.40470	13.72	7.24	0.70	0.53 ± 0.31	56810.87 ± 0.49	33.85 ± 10.69	0.88 ± 0.73	
305	84876	-0.58477	-2.42338	16.63	4.77	5.45	0.13 ± 0.10	56174.14 ± 0.42	21.99 ± 13.00	1.00 ± 0.87	
305	51513	-0.93105	-1.63498	14.52	6.56	1.90	0.00 ± 2.00	56414.19 ± 4.25	93.50 ± 39.03	1.00 ± 0.82	
305	12877	-0.95509	-2.10716	12.98	7.87	0.98	0.38 ± 0.18	56105.26 ± 0.38	20.09 ± 6.09	0.57 ± 0.36	
305	4548	-0.56145	-1.53921	14.58	6.51	1.15	0.51 ± 0.52	56756.77 ± 5.88	110.17 ± 64.66	1.00 ± 1.53	
305	10965	-0.64853	-2.47010	14.11	6.91	0.21	1.28 ± 2.00	56085.19 ± 8.33	39.80 ± 100.18	1.00 ± 8.99	
305	22105	-0.58169	-2.49046	14.89	6.24	1.53	0.20 ± 0.10	56118.50 ± 0.38	63.55 ± 23.34	0.40 ± 0.23	DET.
305	24945	-0.46515	-2.49488	13.48	1.55	2.64	0.25 ± 0.06	56377.50 ± 0.13	24.20 ± 4.39	0.85 ± 0.27	DET.
305	51557	-0.40626	-2.54378	15.11	1.31	1.72	0.00 ± 2.00	56517.13 ± 0.07	17.80 ± 5.87	0.81 ± 0.47	DET.
305	87644	-0.45480	-2.61041	13.46	1.49	0.22	0.96 ± 1.90	55808.57 ± 2.37	55.80 ± 74.65	0.59 ± 2.37	
305	45586	0.04629	-1.98380	14.73	0.93	0.85	0.57 ± 2.00	57262.22 ± 3.16	25.32 ± 296.84	1.00 ± 29.41	
305	76051	-0.45942	-2.21995	13.17	1.12	1.14	0.52 ± 0.41	56141.48 ± 0.91	66.26 ± 36.77	1.00 ± 1.22	DET.
305	57836	-0.13380	-1.64958	14.72	1.25	0.79	0.51 ± 2.00	56739.29 ± 0.39	7.13 ± 315.72	1.00 ± 101.77	DET.
305	79184	-0.04161	-1.69272	16.21	0.95	1.90	0.31 ± 0.58	56841.13 ± 0.48	5.47 ± 6.73	0.79 ± 1.94	DET.
305	87146	0.09125	-1.87919	13.12	1.10	0.39	0.58 ± 0.35	55799.12 ± 0.94	39.08 ± 14.99	0.44 ± 0.43	DET.
305	78425	0.19782	-1.69504	13.78	1.16	0.29	0.01 ± 0.05	56375.90 ± 0.43	166.71 ± 738.34	0.00 ± 0.02	
305	83270	0.16365	-2.24116	14.99	1.01	1.93	0.00 ± 0.00	56370.22 ± 0.12	750.00 ± 1053.09	0.01 ± 0.01	DET.
305	52035	-0.30808	-1.99248	16.27	0.82	3.59	0.14 ± 0.07	56170.20 ± 0.26	32.14 ± 10.55	0.62 ± 0.32	DET.
305	96244	0.07972	-2.07456	14.35	0.97	0.32	0.23 ± 1.68	56610.03 ± 10.80	67.30 ± 69.96	0.54 ± 1.70	DET.
305	18925	0.16883	-2.48300	14.59	1.24	0.88	0.58 ± 0.49	55800.69 ± 1.34	58.23 ± 31.57	1.00 ± 1.35	DET.
319	21482	0.04500	-1.39533	14.64	1.32	2.77	0.24 ± 0.37	56368.42 ± 0.13	10.38 ± 12.12	1.00 ± 1.87	
319	75363	0.13492	-1.13231	14.40	1.65	3.02	0.24 ± 0.13	55808.19 ± 0.94	29.76 ± 8.42	1.00 ± 0.60	DET.
319	81852	0.12729	-1.14514	12.37	1.72	0.47	0.18 ± 0.17	55827.51 ± 1.92	124.93 ± 93.18	0.10 ± 0.11	DET.
319	3050	0.16601	-0.44743	13.79	4.88	11.59	0.03 ± 0.03	57245.48 ± 0.45	248.58 ± 174.11	0.47 ± 0.37	
319	19761	0.10893	-0.49540	15.04	4.42	0.59	0.47 ± 1.65	56866.31 ± 1.03	22.11 ± 31.06	1.00 ± 4.00	
319	29885	0.06187	-0.52356	13.78	4.65	2.07	0.00 ± 2.00	56469.09 ± 0.09	38.41 ± 8.88	0.53 ± 0.30	
319	47428	-0.27338	-1.07622	13.23	2.11	1.96	0.29 ± 0.05	56897.46 ± 0.54	62.39 ± 6.11	0.76 ± 0.16	DET.
319	87262	-0.28093	-1.14837	13.82	1.61	2.08	0.16 ± 0.14	56522.87 ± 0.37	19.14 ± 6.81	0.75 ± 0.50	DET.
319	95634	0.19390	-1.35658	13.54	1.84	0.61	0.12 ± 0.30	55844.46 ± 1.74			

Table 2 — Continued

Tile	ID	l (deg.)	b (deg.)	K_s (mag)	$J - K$ (mag)	Amp	u_0	t_0 (MJD)	t_E (days)	f_{bl}	Comment
319	53886	-0.10963	-0.90446	13.58	2.15	0.61	0.00 ± 2.00	56179.94 ± 0.99	20.58 ± 8.78	1.00 ± 0.89	
319	6989	-0.93746	-0.45560	14.67	6.43	1.73	0.00 ± 2.00	56184.61 ± 1.29	27.62 ± 9.47	0.96 ± 0.67	
319	79778	-1.00800	-0.95836	13.14	7.73	1.46	0.26 ± 0.09	56131.21 ± 0.28	8.93 ± 1.98	0.55 ± 0.26	
319	87060	-0.93844	-0.97172	12.95	7.89	0.46	0.00 ± 2.00	56861.64 ± 4.12	24.27 ± 14.89	0.23 ± 0.43	
319	3547	-0.27303	-0.44503	12.71	8.10	0.75	0.32 ± 0.24	57259.82 ± 0.42	36.72 ± 17.98	0.41 ± 0.39	
319	8718	-0.54848	-1.00606	13.45	7.47	1.76	0.28 ± 0.13	56507.59 ± 0.23	12.70 ± 4.02	0.65 ± 0.39	
319	95579	-0.57219	-1.16388	13.24	7.64	0.35	0.99 ± 1.13	56851.67 ± 1.15	52.72 ± 40.65	1.00 ± 2.36	
319	3978	-0.50597	-0.44617	16.77	4.64	3.49	0.06 ± 0.71	55359.28 ± 1.27	97.17 ± 155.95	1.00 ± 2.65	
319	49598	-1.04837	-1.08947	14.81	6.31	6.51	0.08 ± 0.05	56793.35 ± 0.49	48.94 ± 15.19	1.00 ± 0.45	
319	59552	-0.91198	-1.10962	12.93	7.91	0.43	0.84 ± 1.39	56431.84 ± 2.73	32.45 ± 29.84	1.00 ± 3.06	
319	68573	-0.51615	-0.75423	15.92	5.37	1.66	0.00 ± 2.00	56889.59 ± 1.98	24.28 ± 40.59	0.18 ± 0.43	
319	29850	-1.02870	-0.68188	15.19	5.99	1.58	0.08 ± 0.07	56186.79 ± 1.98	84.41 ± 35.71	0.22 ± 0.14	
319	38669	-1.03987	-0.69888	15.03	6.13	0.82	0.24 ± 0.32	56800.29 ± 2.19	42.95 ± 41.07	0.24 ± 0.41	
319	81917	-0.91565	-0.78509	13.94	7.05	1.67	0.39 ± 0.07	56812.45 ± 0.50	70.14 ± 8.45	1.00 ± 0.26	
319	19250	-0.84143	-1.02642	13.95	7.04	0.70	0.00 ± 2.00	56135.02 ± 0.07	6.90 ± 0.81	1.00 ± 0.22	
319	90727	-0.78873	-1.16034	13.77	7.19	0.23	1.19 ± 2.00	56441.84 ± 3.81	69.97 ± 115.95	1.00 ± 5.57	
319	38914	-0.82286	-1.42640	14.16	6.87	1.10	0.19 ± 0.17	56170.63 ± 0.83	50.60 ± 18.41	0.47 ± 0.33	
319	79079	-0.85193	-1.49861	16.69	4.71	4.95	0.00 ± 0.02	56887.66 ± 0.42	750.00 ± 8127.74	0.01 ± 0.09	DET.
319	102314	-0.86366	-1.54145	13.55	7.38	0.30	0.91 ± 2.00	55813.18 ± 3.16	38.35 ± 243.61	0.72 ± 13.22	
319	5331	-0.77071	-0.81517	12.30	8.45	0.31	0.04 ± 0.07	56123.62 ± 1.15	49.76 ± 77.66	0.02 ± 0.03	
319	33050	-0.71690	-0.86786	13.65	7.30	0.37	0.94 ± 2.00	56153.75 ± 0.99	8.41 ± 12.59	1.00 ± 4.64	
319	80490	-1.19889	-0.96551	13.05	7.80	0.41	0.15 ± 0.05	56327.44 ± 3.55	387.16 ± 80.24	0.08 ± 0.03	
319	16915	0.08345	-0.83682	12.57	2.96	3.47	0.15 ± 0.01	56137.23 ± 0.05	21.96 ± 1.22	0.86 ± 0.08	
319	30059	0.16936	-0.86199	13.84	2.48	0.68	0.27 ± 0.28	55836.77 ± 0.76	24.08 ± 17.45	0.27 ± 0.35	
319	40061	0.18045	-0.88065	12.28	3.04	0.52	0.16 ± 0.48	56551.22 ± 0.89	18.57 ± 8.75	0.38 ± 0.42	
319	55195	0.15508	-0.90955	13.84	2.20	0.43	0.81 ± 1.72	56498.58 ± 0.84	19.24 ± 23.76	1.00 ± 3.82	
319	55412	0.04249	-0.90998	14.34	1.71	0.73	0.00 ± 2.00	55364.21 ± 2.28	29.03 ± 20.84	1.00 ± 1.49	
319	1611	-0.18819	-1.35974	16.19	0.79	13.23	0.00 ± 0.01	55388.41 ± 0.18	750.00 ± 2191.94	0.05 ± 0.16	
319	3488	-0.22720	-1.36323	16.36	4.96	6.52	0.00 ± 2.00	55398.73 ± 3.47	44.95 ± 72.41	1.00 ± 2.41	DET.
319	16104	-0.14236	-1.38481	14.40	1.50	1.04	0.42 ± 0.31	56071.07 ± 3.13	58.45 ± 22.35	1.00 ± 0.97	DET.
319	38154	-0.29430	-1.42327	14.32	1.24	0.45	0.55 ± 2.00	55366.95 ± 3.14	24.10 ± 45.29	1.00 ± 5.66	
319	101943	0.00588	-0.81570	16.62	1.38	5.06	0.00 ± 2.00	55377.47 ± 6.32	750.00 ± 2627.19	0.05 ± 0.19	
319	51595	-0.43142	-0.71629	14.27	3.27	1.63	0.39 ± 0.70	56488.37 ± 2.06	14.97 ± 16.18	1.00 ± 2.60	
319	70966	-0.39831	-0.75228	14.90	6.24	2.05	0.18 ± 0.12	56792.55 ± 0.49	37.61 ± 13.54	0.61 ± 0.38	
319	87886	-0.39165	-0.78417	15.28	1.99	1.39	0.00 ± 2.00	56889.73 ± 1.26	21.75 ± 22.36	0.19 ± 0.29	
319	102369	-0.56143	-1.53920	14.61	6.48	1.21	0.24 ± 0.07	56758.03 ± 2.01	191.44 ± 34.05	0.37 ± 0.12	DET.
319	10859	-0.75308	-0.64291	15.51	5.72	6.45	0.05 ± 0.04	56189.52 ± 2.18	44.61 ± 20.37	1.00 ± 0.77	
319	27112	0.04135	-1.03979	13.94	1.65	1.97	0.23 ± 0.52	55399.88 ± 1.52	29.47 ± 32.79	1.00 ± 2.13	
319	11870	-0.34414	-0.46156	14.70	6.40	3.87	0.00 ± 2.00	56566.44 ± 0.06	38.23 ± 5.63	0.66 ± 0.15	
319	63316	-0.36026	-0.56140	14.98	6.17	0.89	0.24 ± 0.13	56871.16 ± 3.41	189.97 ± 75.60	0.27 ± 0.19	
319	57363	-0.74284	-0.55253	14.33	6.72	0.42	0.93 ± 2.00	55847.21 ± 18.51	70.51 ± 158.91	1.00 ± 7.49	
319	8202	-1.05960	-0.45776	14.08	6.93	2.18	0.21 ± 0.36	55368.37 ± 2.12	64.86 ± 43.11	1.00 ± 1.35	
319	11838	-1.11256	-0.46606	13.16	7.72	0.30	0.31 ± 0.32	56626.80 ± 5.04	112.49 ± 43.93	0.25 ± 0.24	
319	12120	-1.06012	-0.46627	14.25	6.79	0.94	0.60 ± 1.17	55373.41 ± 3.28	64.04 ± 79.50	1.00 ± 3.15	
319	17191	-1.20267	-0.47822	14.58	6.51	1.22	0.31 ± 0.26	57211.60 ± 9.31	68.93 ± 32.93	0.68 ± 0.85	
319	27358	-1.18493	-0.50014	11.83	8.84	0.81	0.53 ± 0.37	56377.24 ± 1.78	38.47 ± 17.20	0.75 ± 0.84	
347	27705	-1.22849	1.32329	13.56	7.37	0.43	0.89 ± 1.33	57251.02 ± 0.49	9.90 ± 9.76	1.00 ± 2.96	DET.
347	65904	-0.82823	1.24752	13.74	7.22	2.97	0.15 ± 0.05	56547.31 ± 0.08	10.51 ± 1.69	1.00 ± 0.29	
347	69960	-0.78207	1.23871	13.65	7.30	0.55	0.82 ± 0.86	56141.68 ± 0.65	13.68 ± 9.16	1.00 ± 2.00	
347	28677	-0.86148	1.13687	15.16	6.02	1.34	0.46 ± 0.32	56138.18 ± 0.58	19.75 ± 8.39	1.00 ± 1.00	
347	44270	-0.85012	1.10457	11.90	8.78	0.39	0.98 ± 1.65	56518.70 ± 1.66	53.48 ± 61.50	1.00 ± 3.49	
347	50357	-0.70073	1.09192	15.07	6.09	1.33	0.26 ± 0.12	56134.30 ± 0.56	55.50 ± 17.96	0.46 ± 0.27	
347	90728	-0.45960	1.57430	13.44	7.47	0.68	0.57 ± 0.42	56099.64 ± 1.03	29.82 ± 14.49	0.70 ± 0.83	DET.
347	69362	-1.18526	1.41394	14.21	6.82	2.82	0.08 ± 0.07	56822.72 ± 0.11	14.27 ± 2.21	0.92 ± 0.25	DET.
347	50028	-1.21774	0.90168	14.62	6.48	0.59	0.24 ± 0.27	57248.58 ± 0.30	9.74 ± 7.89	0.19 ± 0.25	
347	45377	-0.78496	1.47771	13.80	7.17	0.54	0.47 ± 0.50	56867.17 ± 1.10	39.89 ± 22.39	0.62 ± 0.87	DET.
347	41875	-0.74337	0.91837	15.42	5.79	2.31	0.05 ± 0.11	56062.46 ± 1.56	129.53 ± 32.61	0.62 ± 0.25	
347	49702	-0.70991	0.89991	13.72	7.24	6.11	0.12 ± 0.06	56169.68 ± 0.46	22.39 ± 5.32	1.00 ± 0.45	
347	22839	-0.90341	1.51525	15.17	6.01	1.29	0.06 ± 0.10	56834.96 ± 1.03	236.52 ± 375.49	0.07 ± 0.13	DET.
347	38514	-0.94772	0.92390	13.67	7.28	0.78	0.52 ± 0.17	56554.34 ± 0.31	17.30 ± 3.64	0.68 ± 0.35	
347	48421	-1.03510	0.90071	15.21	5.97	0.98	0.54 ± 0.78	57259.26 ± 0.93	21.71 ± 21.64	1.00 ± 2.28	
347	16027	-0.66306	0.97723	14.37	6.68	0.70	0.67 ± 1.72	56205.40 ± 1.78	10.70 ± 13.77	1.00 ± 4.29	
347	25797	-1.04459	1.14102	13.90	7.08	2.60	0.29 ± 0.04	56167.85 ± 0.17	34.97 ± 2.94	1.00 ± 0.16	
347	34396	-1.01718	1.12279	14.61	6.48	1.76	0.28 ± 0.10	56134.96 ± 0.27	28.61 ± 6.80	0.72 ± 0.33	
347	5981	-0.56564	1.73438	14.07	6.94	8.91	0.10 ± 0.01	56102.96 ± 0.02	14.14 ± 1.28	1.00 ± 0.14	DET.
347	82999	-0.56626	1.02288	15.83	5.45	6.94	0.08 ± 0.04	56536.81 ± 0.13	34.36 ± 9.64	1.00 ± 0.38	
347	40812	-0.65045	1.30091	13.09	7.77	1.00	0.57 ± 0.16	56516.59 ± 1.43	114.85 ± 21.24	1.00 ± 0.45	
347	41193	0.03728	1.29910	15.32	5.88	1.81	0.39 ± 0.66	56853.05 ± 3.97	57.45 ± 65.74	1.00 ± 2.41	
347	69720	-0.04291	0.68396	14.99	3.34	3.43	0.12 ± 0.04	56576.07 ± 0.32	34.10 ± 8.66	0.52 ± 0.19	
347	92482	0.03445	0.63426	14.13	6.89	5.13	0.15 ± 0.10	57251.00 ± 0.30	34.26 ± 17.98	0.92 ± 0.70	
347	35068	-0.50154	1.12892	14.80	1.82	0.39	0.99 ± 2.00	56178.09 ± 7.67	90.75 ± 124.03	1.00 ± 4.27	
347	72620	-0.37091	1.05774	16.94	4.50	3.60	0.18 ± 0.36	57243.78 ± 0.71	13.38 ± 14.20	1.00 ± 1.95	
347	28089	-0.42203	1.50986	13.73	7.23	0.34	0.25 ± 0.43	57248.53 ± 0.31	5.70 ± 6.57	0.12 ± 0.24	
347	62565	-0.40420	1.44447	12.85	1.74	0.29	0.59 ± 0.52	56113.40 ± 0.21	6.82 ± 3.57	0.34 ± 0.48	
347	83068	-0.39933	1.40547	14.04	1.16	0.59	0.01 ± 0.02	56115.01 ± 0.28	324.86 ± 957.76	0.00	

Table 2 — *Continued*

Tile	ID	l (deg.)	b (deg.)	K_s (mag)	$J - K$ (mag)	Amp	u_0	t_0 (MJD)	t_E (days)	f_{bl}	Comment
347	3785	-0.42851	1.00270	16.14	1.92	1.73	0.36 ± 0.70	56136.46 ± 1.90	26.14 ± 31.35	1.00 ± 2.56	
347	18360	-0.05394	1.52645	15.10	6.07	0.57	0.09 ± 0.07	56827.30 ± 3.37	369.03 ± 206.61	0.06 ± 0.04	
347	21146	0.04363	1.52078	14.73	6.38	0.64	0.55 ± 1.60	57249.48 ± 0.23	4.79 ± 8.10	0.76 ± 3.35	
347	61846	-0.07325	1.44093	14.96	1.48	0.71	0.41 ± 0.86	56202.00 ± 1.53	19.65 ± 27.17	0.42 ± 1.24	
347	75581	-0.01650	1.41358	14.89	6.24	4.85	0.08 ± 0.02	56212.16 ± 1.90	117.91 ± 20.14	0.47 ± 0.14	
347	75845	-0.04066	1.41306	13.91	1.43	5.01	0.13 ± 0.02	56123.79 ± 0.02	3.89 ± 0.41	1.00 ± 0.16	
347	21402	0.00616	0.96843	13.20	1.75	0.92	0.54 ± 2.00	56498.69 ± 4.68	6.81 ± 20.76	1.00 ± 10.10	
347	68700	0.03206	0.87129	13.70	7.26	0.82	0.61 ± 0.98	57247.63 ± 0.20	3.59 ± 3.63	1.00 ± 2.62	
347	39402	-0.22791	0.93399	13.43	7.49	0.17	0.18 ± 0.14	56115.49 ± 0.88	61.17 ± 35.99	0.04 ± 0.03	
347	72106	-0.27629	0.86957	13.73	1.49	0.65	0.49 ± 2.00	55807.67 ± 0.89	16.18 ± 31.14	1.00 ± 5.27	
347	51199	0.16339	1.46328	14.64	1.63	2.52	0.29 ± 0.05	56101.02 ± 0.28	47.87 ± 5.45	1.00 ± 0.21	
347	44668	0.19562	0.92445	12.67	1.89	0.34	0.34 ± 1.88	56733.61 ± 8.45	79.68 ± 84.73	1.00 ± 3.43	
347	57724	0.06212	0.89838	14.33	6.72	1.66	0.28 ± 0.25	57239.30 ± 0.15	10.35 ± 4.66	1.00 ± 0.92	
347	87437	0.12963	0.83843	14.69	2.21	0.90	0.61 ± 0.56	56566.02 ± 1.28	36.40 ± 20.83	1.00 ± 1.48	
347	7923	-0.27876	1.17927	13.65	7.30	1.45	0.10 ± 0.44	56831.99 ± 0.53	8.30 ± 10.91	0.31 ± 0.72	
347	76798	0.11414	1.58643	13.53	1.56	0.31	1.08 ± 2.00	56188.78 ± 2.18	28.44 ± 38.56	1.00 ± 4.47	
347	50518	0.12593	1.09631	11.86	8.82	0.81	0.68 ± 0.50	55877.24 ± 15.06	333.28 ± 143.49	1.00 ± 1.25	
347	35700	-0.23557	1.31220	13.04	1.75	1.33	0.23 ± 0.03	56208.96 ± 1.14	75.24 ± 6.34	0.40 ± 0.07	
347	39564	-0.27058	1.30506	12.42	1.83	0.23	0.84 ± 2.00	56183.67 ± 0.16	3.91 ± 6.68	1.00 ± 5.66	
347	82357	-0.17561	1.22425	13.15	1.99	0.94	0.43 ± 0.14	56023.72 ± 1.60	57.66 ± 10.67	0.82 ± 0.38	
347	94666	-0.24569	0.63450	16.10	5.21	3.32	0.02 ± 0.02	57248.37 ± 0.93	750.00 ± 589.38	0.07 ± 0.06	
347	18361	0.17027	0.79111	13.05	2.77	0.41	0.91 ± 1.11	56201.32 ± 1.82	22.43 ± 16.96	1.00 ± 2.42	
347	51805	0.11390	0.72254	14.13	2.60	2.11	0.27 ± 0.25	55821.68 ± 1.91	89.87 ± 63.45	0.64 ± 0.74	
347	52306	0.11364	0.72152	14.90	2.59	1.41	0.06 ± 0.13	55815.24 ± 2.27	124.77 ± 236.99	0.09 ± 0.20	
347	52578	0.11422	0.72098	14.19	2.47	0.45	0.75 ± 2.00	55808.24 ± 1.60	20.87 ± 86.28	1.00 ± 11.65	
347	76171	0.06529	0.67171	14.44	3.06	0.91	0.47 ± 0.26	56534.89 ± 0.46	27.08 ± 9.37	0.73 ± 0.59	
347	85434	0.13499	0.65202	15.06	6.10	1.95	0.27 ± 0.24	57253.81 ± 0.34	11.93 ± 5.88	1.00 ± 0.98	
361	56975	-1.16291	2.35824	12.35	8.40	0.34	0.00 ± 2.00	56878.28 ± 1.08	36.32 ± 7.67	0.28 ± 0.12	DET.
361	76350	-1.16879	2.32008	13.48	7.44	0.25	0.07 ± 0.07	56557.69 ± 0.77	39.47 ± 30.03	0.02 ± 0.02	
361	1531	-1.12199	1.91578	16.46	4.91	4.79	0.00 ± 2.00	56000.07 ± 0.42	28.13 ± 38.00	1.00 ± 2.07	
361	41821	-1.09120	2.75287	12.05	8.66	0.22	1.19 ± 2.00	55995.26 ± 1.14	16.35 ± 77.04	1.00 ± 15.11	
361	12561	-1.09206	2.26178	14.45	6.62	1.47	0.42 ± 0.10	56805.57 ± 0.18	20.36 ± 3.27	0.93 ± 0.33	DET.
361	10285	-0.73004	2.26764	13.78	7.18	0.14	1.41 ± 2.00	55996.67 ± 1.16	9.71 ± 95.03	1.00 ± 34.25	
361	52033	-0.75845	2.19113	13.46	7.46	0.19	0.22 ± 0.34	55826.42 ± 2.38	73.90 ± 89.76	0.05 ± 0.09	
361	97832	-0.47548	2.65704	17.19	4.28	4.43	0.00 ± 2.00	56002.03 ± 0.64	75.50 ± 86.87	0.20 ± 0.27	
361	5197	-1.05840	2.09186	13.66	7.29	0.23	0.02 ± 0.03	55998.29 ± 0.81	298.13 ± 376.61	0.01 ± 0.01	
361	38445	-1.07630	2.02557	14.27	6.77	0.39	0.00 ± 2.00	55998.25 ± 1.02	6.25 ± 34.42	1.00 ± 18.12	
361	21718	-0.80340	2.06324	17.30	4.19	9.42	0.00 ± 2.00	57230.88 ± 2.14	53.12 ± 82.17	1.00 ± 2.31	
361	62342	-0.68267	1.99040	13.66	7.29	0.29	1.05 ± 2.00	55993.98 ± 1.06	11.16 ± 29.41	1.00 ± 8.24	
361	87414	-0.78409	1.94430	13.57	7.36	2.69	0.00 ± 2.00	56559.44 ± 0.46	27.60 ± 14.54	0.37 ± 0.27	DET.
361	14405	-0.93416	2.62554	16.02	5.29	5.43	0.05 ± 0.07	56177.45 ± 1.50	23.03 ± 7.58	0.76 ± 0.51	
361	21506	-0.87720	2.61239	13.31	7.59	0.32	0.00 ± 2.00	55998.95 ± 0.81	9.90 ± 135.11	0.39 ± 14.43	
361	4300	-1.03976	2.27743	13.61	7.33	0.41	0.90 ± 2.00	55993.34 ± 1.28	18.76 ± 48.60	1.00 ± 7.35	
361	53577	-0.88740	2.18240	16.58	4.81	1.22	0.50 ± 0.77	56126.72 ± 1.16	15.13 ± 14.75	1.00 ± 2.35	
361	43137	-0.51274	2.75734	15.18	6.00	1.14	0.50 ± 0.40	56837.67 ± 0.86	26.41 ± 13.66	1.00 ± 1.20	
361	50705	-0.60138	2.19309	14.38	6.68	1.23	0.09 ± 0.05	57169.25 ± 2.20	61.30 ± 26.57	0.16 ± 0.12	DET.
361	15874	-0.95946	2.44027	13.23	7.65	0.26	1.03 ± 1.90	56758.88 ± 4.13	47.75 ± 54.17	0.88 ± 3.34	DET.
361	22926	-0.95717	2.42706	13.48	7.45	0.50	0.80 ± 1.19	57239.72 ± 0.45	12.76 ± 12.12	1.00 ± 2.77	DET.
361	21529	-0.91129	1.87798	15.80	5.47	1.15	0.50 ± 2.00	56007.24 ± 2.90	21.22 ± 103.87	1.00 ± 11.86	
361	12353	-0.68595	2.44860	16.73	4.68	2.98	0.26 ± 0.26	56202.52 ± 2.38	55.58 ± 39.73	0.80 ± 0.99	
361	98676	-0.66323	2.28986	15.67	5.58	7.70	0.07 ± 0.02	56152.77 ± 0.10	37.47 ± 7.00	0.56 ± 0.14	
361	18788	-0.46625	2.43707	16.99	1.39	2.49	0.23 ± 0.14	56140.04 ± 0.50	28.63 ± 12.22	0.69 ± 0.51	
361	32613	-0.33669	1.85856	14.27	1.57	0.58	0.69 ± 0.46	56139.12 ± 0.85	35.84 ± 15.06	0.82 ± 0.95	
361	22795	-0.01716	1.87776	12.67	1.50	3.15	0.08 ± 0.03	56193.99 ± 0.04	17.47 ± 1.38	0.97 ± 0.13	
361	46457	-0.40727	2.20140	13.97	1.41	0.26	0.93 ± 2.00	57244.00 ± 0.48	8.67 ± 36.59	1.00 ± 14.21	
361	18865	-0.04031	2.25114	14.23	1.72	0.51	0.00 ± 2.00	56770.51 ± 2.48	24.43 ± 15.77	1.00 ± 1.53	
361	27218	-0.10863	2.23468	14.47	1.62	0.52	0.84 ± 2.00	56822.08 ± 1.98	6.10 ± 22.86	1.00 ± 12.09	
361	43970	0.01860	2.20288	16.77	1.31	7.08	0.00 ± 2.00	57234.07 ± 3.84	750.00 ± 2430.72	0.02 ± 0.06	
361	10581	-0.40728	2.63586	13.36	1.29	0.21	1.27 ± 2.00	56798.55 ± 4.78	10.08 ± 30.46	1.00 ± 11.43	
361	8362	-0.40087	2.08736	14.29	1.57	4.13	0.09 ± 0.08	56577.86 ± 1.45	45.75 ± 15.81	0.46 ± 0.30	
361	49925	-0.32015	2.01253	13.88	1.73	2.10	0.33 ± 0.08	56828.54 ± 0.09	18.57 ± 2.75	1.00 ± 0.31	
361	15164	-0.09392	2.07512	12.25	1.70	1.06	0.53 ± 0.09	56006.97 ± 1.07	102.38 ± 10.42	1.00 ± 0.27	
361	75500	-0.00028	1.95998	14.89	1.37	0.79	0.00 ± 2.00	55769.35 ± 2.68	34.06 ± 9.86	1.00 ± 0.67	
361	80391	0.00243	1.95050	10.96	1.69	2.59	0.00 ± 2.00	56120.01 ± 0.36	93.04 ± 115.93	0.10 ± 0.15	
361	67302	-0.15211	2.16101	16.21	1.41	1.98	0.00 ± 2.00	56816.24 ± 0.99	10.87 ± 8.17	1.00 ± 1.57	
361	21040	-0.20217	1.88149	13.91	1.44	1.23	0.49 ± 0.52	56567.46 ± 0.38	12.92 ± 8.65	1.00 ± 1.63	
361	106680	-0.14401	1.72347	15.64	1.40	1.83	0.32 ± 0.50	56541.75 ± 1.12	18.52 ± 16.22	1.00 ± 1.87	
361	58222	0.20321	1.81015	13.48	1.37	0.96	0.25 ± 0.10	56063.92 ± 1.06	$67.04 \pm$		

Table 2 — *Continued*

Tile	ID	l (deg.)	b (deg.)	K_s (mag)	$J - K$ (mag)	Amp	u_0	t_0 (MJD)	t_E (days)	f_{bl}	Comment
375	79774	-0.65186	3.41172	13.98	7.02	0.20	1.24 ± 2.00	56789.67 ± 4.09	36.73 ± 132.14	1.00 ± 12.20	DET.
375	8388	-0.09215	3.36281	17.25	4.24	1.68	0.21 ± 0.52	56113.79 ± 1.01	21.02 ± 18.98	1.00 ± 1.83	
375	42857	-0.48704	3.11487	16.96	4.48	2.76	0.28 ± 0.25	56188.07 ± 0.47	13.80 ± 8.56	1.00 ± 1.17	
375	23711	0.06360	3.69847	13.28	7.61	0.93	0.00 ± 2.00	55988.93 ± 1.05	65.53 ± 280.05	0.03 ± 0.16	
375	72168	0.24988	3.05546	16.72	4.69	5.05	0.00 ± 2.00	55995.52 ± 0.22	47.98 ± 40.19	1.00 ± 1.25	
375	80484	0.25066	3.03874	12.93	7.91	2.86	0.25 ± 0.13	55809.82 ± 0.71	72.64 ± 29.85	1.00 ± 0.65	DET.
375	23911	0.06543	3.51626	14.55	6.53	0.74	0.18 ± 0.39	56005.30 ± 1.62	30.45 ± 49.30	0.16 ± 0.42	
375	90864	0.06159	3.38532	16.63	4.77	7.59	0.00 ± 2.00	55990.01 ± 0.85	20.16 ± 27.17	1.00 ± 2.50	
375	54167	0.07092	2.90685	13.66	7.29	0.30	0.70 ± 2.00	55998.94 ± 0.47	7.94 ± 135.85	1.00 ± 56.03	
375	35747	-1.05529	3.12250	14.22	6.81	0.73	0.66 ± 2.00	57156.71 ± 135.42	64.06 ± 300.15	1.00 ± 17.69	DET.
375	83454	-0.84046	3.59040	16.23	5.11	2.58	0.00 ± 2.00	55998.09 ± 0.36	90.22 ± 89.83	0.17 ± 0.20	
375	104369	-0.85058	3.55138	16.36	4.99	1.70	0.37 ± 1.28	56821.12 ± 1.67	12.28 ± 23.19	1.00 ± 4.37	
375	33561	-0.79048	3.13094	13.35	7.55	0.63	0.75 ± 0.83	55828.49 ± 3.15	47.26 ± 33.76	1.00 ± 2.02	DET.
375	44220	-0.87302	3.83148	13.61	7.33	1.94	0.34 ± 0.38	56824.25 ± 1.12	6.34 ± 3.75	1.00 ± 1.71	DET.
375	102238	-0.35875	3.37052	14.51	6.56	1.38	0.00 ± 2.00	55999.57 ± 0.36	30.11 ± 48.04	0.32 ± 0.77	
375	82376	-0.38249	2.86060	14.02	6.99	0.35	0.42 ± 0.37	56081.79 ± 4.93	64.92 ± 33.39	0.20 ± 0.26	DET.
375	24001	0.05155	3.51611	13.96	7.03	1.23	0.28 ± 0.09	56866.84 ± 0.28	52.73 ± 6.56	1.00 ± 0.28	
375	73190	0.00278	3.42125	16.82	4.60	3.33	0.23 ± 0.22	56795.27 ± 3.63	67.86 ± 43.14	1.00 ± 1.22	DET.
375	65654	-0.42227	3.62051	14.54	6.54	0.29	0.52 ± 2.00	56877.25 ± 23.26	19.73 ± 207.05	1.00 ± 40.03	

[‡]One standard deviation errors are presented along each parameter obtained from the microlensing model fitting procedure

[§]Typical positional errors are 0.1 arcsec (Smith et al. 2018).

[¶]Typical photometric errors are $\sigma_{K_s} = 0.01$ mag, and $\sigma_{J,H} = 0.03$ mag (Saito et al. 2012; Contreras Ramos et al. 2017; Alonso-García et al. 2018).